Magnetism and superconductivity in the layered hexagonal transition metal pnictides

Jinfeng Zeng,[1,2] Shengshan Qin,[1,2] Congcong Le,[1,3] and Jiangping Hu[1,3,4,*]

[1]*Beijing National Laboratory for Condensed Matter Physics and Institute of Physics, Chinese Academy of Sciences, Beijing 100190, China*

[2]*School of Physical Sciences, University of Chinese Academy of Sciences, Beijing 100049, China*

[3]*Kavli Institute of Theoretical Sciences, University of the Chinese Academy of Sciences, Beijing 100190, China*

[4]*Collaborative Innovation Center of Quantum Matter, Beijing, China*

(Received 24 September 2017; revised manuscript received 2 November 2017; published 14 November 2017)

We investigate the electronic and magnetic structures of the 122 (AM_2B_2) hexagonal transition metal pnictides with A = (Sr, Ca), M = (Cr, Mn, Fe, Co, Ni), and B = (As, P, Sb). It is found that the family of materials shares critical similarities with those of tetragonal structures that include the famous iron-based high-temperature superconductors. In both families, the next-nearest-neighbor (NNN) effective antiferromagnetic (AFM) exchange couplings reach the maximum value in the iron-based materials. While the NNN couplings in the latter are known to be responsible for the C-type AFM state and to result in the extended s-wave superconducting state upon doping, they cause the former to be extremely frustrated magnetic systems and can lead to a time-reversal symmetry-broken $d + id$ superconducting state upon doping. Thus, if synthesized, iron-based compounds with hexagonal structure can help us to determine the origin of high-temperature superconductivity.

DOI: 10.1103/PhysRevB.96.174506

I. INTRODUCTION

The accidental discovery of iron-based superconductors in 2008 [1] was a great surprise to the entire high-temperature (high-T_c) superconductivity research community. Since then, iron-based superconductors have been one of the most active research fields in condensed-matter physics. It was wildly cheered that the study of these materials might eventually lead us to understand the superconducting mechanism of unconventional high-temperature superconductors. Nevertheless, even if many rich physics in these materials have been discovered and well understood, the superconductivity mechanism remains a controversial subject.

Theoretically, to understand high-T_c superconductivity, different electronic properties or phenomena have been selected and emphasized in different approaches and models [2]. The essential difficulty in solving the high-T_c mechanism lies in how to identify indispensable features that are directly tied to high-T_c superconductivity among complex electronic structure and physical phenomena. In principle, successful identification should also lead us to predict new families of high-T_c superconductors.

If we assume that there should be one unified superconducting mechanism for unconventional high-temperature superconductors including cuprates [3], it is possible to make the identification by comparing different classes of materials. Considering the 122 family of iron-based superconductors, the iron atoms can be fully replaced by other transition metal atoms, such as Cr, Mn, Co, Ni, and Cu. These compounds have the same lattice structures as the 122 iron-based superconductors. Accumulating experimental evidence [4–13] suggests that they do not exhibit high-T_c superconductivity. These facts lead us to ask a profound question: why is iron so special for high T_c superconductivity?

If we compare all these similar materials, only the iron-based materials exhibit C-type antiferromagnetic (AFM) order [14], and the superconductivity emerges when the magnetic order is suppressed. The C-type AFM state indicates the presence of strong effective AFM exchange couplings between two next-nearest-neighbor (NNN) iron atoms. The NNN AFM couplings are known to stem from the superexchange mechanism through the couplings between the t_{2g} iron d orbitals and the anion p orbitals. In many previous theoretical studies [15–17], these AFM interactions were shown to generate strong superconducting pairings with extended s-wave symmetry. Recently, we also pointed out that the d^6 configuration at Fe^{2+} is a unique configuration to isolate the t_{2g} orbitals near Fermi energy [18,19]. Thus, the special electronic structure in which the t_{2g} orbitals are isolated near Fermi energy to generate the maximum superexchange AFM interactions in the vicinity of the d^6 configuration at Fe^{2+} is suggested to be the key to the high-T_c mechanism. This speciality is also satisfied in cuprates [3], in which the single $d_{x^2-y^2}$ e_g orbital of Cu^{2+} which is responsible for the superexchange interactions is isolated near Fermi energy.

In this paper, we argue that the hexagonal 122 transition metal pnictides, AM_2B_2, with A = (Sr, Ca), M = (Cr, Mn, Fe, Co, Ni), and B = (As, P, Sb), which have trigonal $CaAl_2Si_2$-type structure, could be a new family of materials to test the above identification of the superconducting mechanism. We compare the magnetic properties between the tetragonal and hexagonal 122 families of pnictides obtained from density functional theory (DFT) calculations and find that the overall trend of magnetism in the hexagonal structure with the change of transition metal atoms is very similar to the one in the tetragonal structure. Their similarities include the following: (1) the NNN AFM exchange interactions reach maximum in Fe-based materials, (2) the nearest-neighbor (NN) AFM interactions, which are mainly attributed to the direct magnetic exchange mechanism, are very strong in Cr/Mn-based materials, and (3) in Co/Ni/Cu-based materials, magnetic interactions are very weak or negligible. Because of the strong NNN AFM interactions, the iron-based hexagonal materials are extremely frustrated magnetic systems. Their electronic structure near Fermi energy is mainly attributed to t_{2g} orbitals that form

*jphu@iphy.ac.cn

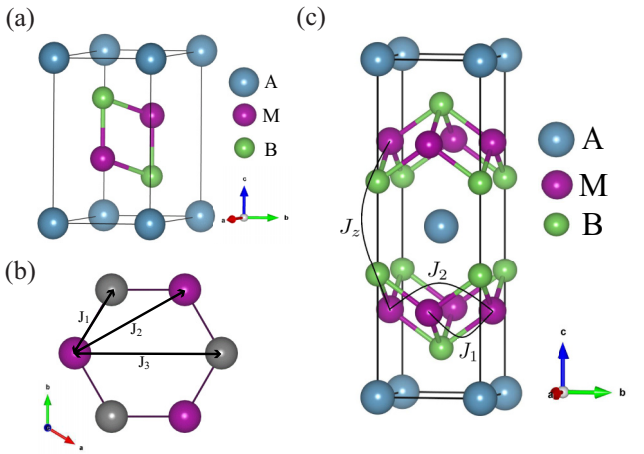

FIG. 1. (a) The crystal structure of the hexagonal AM_2B_2 (A = Sr, Ca; M = Cr, Mn, Fe, Co, Ni; B = As, P, Sb) with the trigonal $CaAl_2Si_2$-type structure (space group $P\bar{3}m1$, No. 164). (b) The corrugated honeycomb lattice formed only by the M atoms in the ab plane. Exchange interactions between NN J_1, NNN J_2, and third NN J_3 are indicated. (c) The crystal structure of AM_2B_2 (A = Ba; M = Cr, Mn, Fe, Co, Ni; B = As, P) with the body-centered-tetragonal structure (space group $I4/mmm$, No. 139). The in-plane NN magnetic exchange interaction J_1, the in-plane NNN exchange interaction J_2, and the out-of-plane NN along the c axis exchange interaction J_z are indicated.

two quasi-two-dimensional electron pockets. Upon doping, the superconductivity with $d + id$ spin-singlet pairing symmetry can be developed.

This paper is organized as follows. In Sec. II, we present the calculation results from DFT and study the crystal structure of hexagonal 122 transition metal pnictides AM_2B_2 (A = Sr, Ca; M = Cr, Mn, Fe, Co, Ni; B = As, P, Sb). In Sec. III, we review and summarize the magnetic properties of the tetragonal family. In Sec. IV, we investigate the effective magnetic exchange interactions in the hexagonal family. In Sec. V, we investigate the pressure effect on the magnetism of the hexagonal $CaFe_2As_2$. In Sec. VI, we discuss the electronic structure of the hexagonal $CaFe_2As_2$ and analyze the possible superconducting state. Finally, in Sec. VIII, we give a summary and provide the main conclusions of our paper.

II. CRYSTAL STRUCTURES AND CALCULATION METHODS

The 122 tetragonal and hexagonal crystal structures are shown in Fig. 1. The 122 iron-based superconductors, such as $BaFe_2As_2$, have a body-centered-tetragonal structure, as shown in Fig. 1(c) with space group $I4/mmm$. Besides iron-based materials, materials with this crystal structure have been synthesized for Cr, Mn, Co, Ni, and Cu. The hexagonal 122 structure is shown in Fig. 1(a). This structure is referred to as the trigonal $CaAl_2Si_2$-type structure with space group $P\bar{3}m1$. (Sr, Ca)Mn_2As_2 with this structure has been synthesized. Here we use the DFT calculations to systematically investigate these families of materials. The 122 tetragonal family has been intensively investigated. The magnetic states have been correctly obtained by the DFT calculations. Although the hexagonal 122 structure has also been investigated, there are no systematic DFT results.

TABLE I. The experimental crystal structure parameters for BaM_2B_2 (M = Cr, Mn, Fe, Co, Ni; B = P, As) with the body-centered-tetragonal structure (space group $I4/mmm$).

	a (Å)	c (Å)	Z_{As}
$BaCr_2As_2$ [25]	3.963	13.600	0.3572
$BaMn_2As_2$ [26]	4.154	13.415	0.3613
$BaFe_2As_2$ [27]	3.963	13.017	0.3545
$BaCo_2As_2$ [25]	3.958	12.670	0.3509
$BaNi_2As_2$ [10]	4.112	11.540	0.3476
$BaFe_2P_2$ [28]	3.840	12.442	0.3456

Our DFT calculations employ the projector augmented-wave (PAW) method encoded in the Vienna Ab initio Simulation Package (VASP) [20–22], and the generalized gradient approximation (GGA) [23] for the exchange-correlation functional is used. We relax the lattice constants and internal atomic positions for the hexagonal family, where the plane-wave cutoff energy is 600 eV and the k points are $13 \times 13 \times 7$. Forces are minimized to less than 0.01 eV/Å in the structural relaxation. Throughout this work, cutoff energies of 500 eV for the tetragonal family and 450 eV for the hexagonal family are taken for expanding the wave functions into the plane-wave basis. The number of these k points is $7 \times 7 \times 3$ for the tetragonal family and $7 \times 11 \times 7$ for the hexagonal family in the calculations of the magnetic structures. The GGA plus on-site repulsion U method (GGA + U) in the formulation of Dudarev *et al.* [24] is employed to describe the associated electron correlation effect.

In the 122 tetragonal family, the A site has a very limited effect on electronic physics. In our calculations and analysis, we let the A site be a Ba atom. We adopt the experimental lattice constants which are shown in Table I, and all those materials have been synthesized. For the hexagonal family, $CaMn_2As_2$, $CaMn_2P_2$, $CaMn_2Sb_2$, $SrMn_2P_2$, and $SrMn_2As_2$ have been synthesized, and their magnetic properties have been studied [29–36]. Like for the tetragonal family structure, the A site atoms have little effect on the electronic and magnetic structure near the Fermi level. In the following, we let the A site be a Ca atom. The trigonal $CaAl_2Si_2$-type structure is shown in Fig. 1(a). The M-site sublattice forms the corrugated honeycomb lattice, which is shown in Fig. 1(b). The purple and gray M atoms belong to the high and low trigonal layers, respectively. The lattice constants are listed in Table II. $CaMn_2As_2$ has been reported with AFM order [33].

TABLE II. Experimental and optimized structural parameters of $CaMn_2B_2$ (B = As, P) using GGA + U (U = 1.5 eV) in the AFM ordered state.

	a (Å)	c (Å)	z_X	z_Y
$CaMn_2As_2$ (experiment) [29]	4.230	7.030	0.6237	0.2557
$CaMn_2As_2$ (relax)	4.258	7.002	0.6203	0.2574
$CaMn_2P_2$ (experiment) [30]	4.096	6.848	0.6246	0.2612
$CaMn_2P_2$ (relax)	4.109	6.775	0.6213	0.2644

TABLE III. The optimized crystal structure parameters for CaM_2B_2 (M = Cr, Mn, Fe, Co, Ni; B = P, As) with the trigonal $CaAl_2Si_2$-type structure (space group $P\bar{3}m1$) using GGA + U (U = 1.5 eV) in the AFM ordered state.

	a (Å)	c (Å)	z_X	z_Y
$CaCr_2As_2$	4.122	7.269	0.6180	0.2553
$CaMn_2As_2$	4.258	7.002	0.6203	0.2574
$CaFe_2As_2$	4.086	6.834	0.6237	0.2740
$CaCo_2As_2$	3.891	6.761	0.6269	0.2894
$CaNi_2As_2$	3.965	6.714	0.6299	0.2869
$CaCr_2P_2$	3.972	7.023	0.6203	0.2630
$CaMn_2P_2$	4.109	6.775	0.6213	0.2644
$CaFe_2P_2$	3.858	6.639	0.6236	0.2859
$CaCo_2P_2$	3.715	6.602	0.6263	0.2973
$CaNi_2P_2$	3.788	6.558	0.6271	0.2919

However, the other materials in CaM_2B_2 (M = Cr, Fe, Co, Ni) have not been synthesized. In order to study their magnetic structures, we relax the lattice constants and internal atomic positions with the GGA + U method in the AFM ordered state. By relaxing the lattice constants and internal atomic positions for $CaMn_2As_2$ and $CaMn_2P_2$ with U = (0.0,0.5,1.0,1.5,2.0,2.5) eV, we find that when U = 1.5 eV, the optimized lattice constants are the closest to the experimental data for both $CaMn_2As_2$ and $CaMn_2P_2$, which are given in Table II. Therefore, we adopt the value U = 1.5 eV to relax the other materials CaM_2As_2 and CaM_2P_2 (M = Cr, Fe, Co, Ni) with the experimental lattice constants of $CaMn_2As_2$ and $CaMn_2P_2$ as the input parameters, respectively. The results of the optimized structural parameters are listed in Table III. In the calculations of the magnetic states of the trigonal $CaAl_2Si_2$-type structure CaM_2B_2, we double the primitive cell as the unit cell (indicated by the red frame in Fig. 4 below).

III. THE MAGNETISM IN THE TETRAGONAL 122 TRANSITION METAL PNICTIDES

In this section, we review and investigate the magnetic properties of the 122 tetragonal BaM_2B_2 (M = Cr, Mn, Fe, Co, Ni; B = As, P). We consider four competing collinear magnetic states, the ferromagnetic (FM) state, the G-type AFM state, and two stripe states. We distinguish the two stripe states as the stripe FM state with ferromagnetic alignment of adjacent spins along the c axis and the C-type AFM state with antiferromagnetic alignment. These four magnetic states are shown in Fig. 2. It is known that the magnetism can be described by the effective J_1-J_2-J_z Heisenberg model [37–42], which is given by

$$H = J_1 \sum_{\langle ij \rangle} \vec{S}_i \cdot \vec{S}_j + J_2 \sum_{\langle\langle ij \rangle\rangle} \vec{S}_i \cdot \vec{S}_j + J_z \sum_{\langle ij \rangle_c} \vec{S}_i \cdot \vec{S}_j, \quad (1)$$

where $\langle ij \rangle$, $\langle\langle ij \rangle\rangle$, and $\langle ij \rangle_c$ denote the summation over the in-plane NN, in-plane NNN, and out-of-plane NN along the c axis, respectively. The exchange interaction parameters J_1, J_2, and J_z are indicated in Fig. 1(c). $\vec{S}_i$ is the spin operator for the ith site. Throughout this paper, a positive J corresponds to an antiferromagnetic interaction, and a negative J corresponds to a ferromagnetic interaction. The classical energies of the above magnetic states are

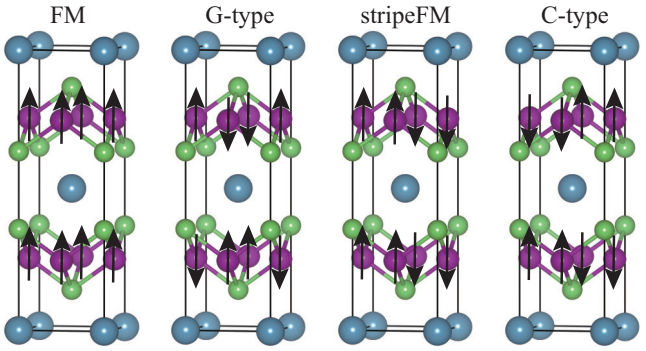

FIG. 2. Sketch of the four collinear magnetic states, including the FM states, the G-type AFM state, the stripe FM state, and the C-type AFM state.

$$\begin{aligned} E_{\mathrm{FM}} &= NS^2(2J_1 + 2J_2 + J_z) + E_0, \\ E_{G-\mathrm{type}} &= NS^2(-2J_1 + 2J_2 - J_z) + E_0, \\ E_{\mathrm{stripeFM}} &= NS^2(-2J_2 + J_z) + E_0, \\ E_{C-\mathrm{type}} &= NS^2(-2J_2 - J_z) + E_0, \end{aligned} \quad (2)$$

where E_0 is the energy of the nonmagnetic state.

We calculate the magnetic moments and the total energies of the above magnetic states with GGA + U. If the calculated local magnetic moments at M sites are very close to each other, we can extract the magnetic exchange coupling constants with Eq. (2). The results show that in $BaCr_2As_2$ the average moments of the four magnetic states vary from $2.3\mu_B$ to $3.4\mu_B$. The values increase when U increases. The magnetic moments do not vary significantly for the above four magnetic states. The average moments vary from $3.5\mu_B$ to $4.1\mu_B$ in $BaMn_2As_2$ and $2.0\mu_B$ to $2.9\mu_B$ in $BaFe_2As_2$. For $BaCo_2As_2$, the moments are very small. Finally, in $BaNi_2As_2$, the moments are zero within the range of error $0.001\mu_B$, and there is no energy gain for magnetic states. These results are consistent with previous calculations [42–52]. For $BaNi_2As_2$, our results are consistent with the angle-resolved photoemission spectroscopy experiment [53], which shows that collinear spin-density-wave magnetic ordering does not exist in $BaNi_2As_2$.

We can extract the magnetic exchange parameters with Eqs. (2). The results are summarized below. For Co-based materials, as the magnetic moment is too small, it is not reliable to extract these exchange parameters. For Ni-based materials, the calculated magnetic exchange parameters are zero. For the other three materials, the results are consistent with previous calculations as well as experimental measurements. As the energy gain in the magnetic state is proportional to $J\langle S \rangle^2$ and the ordered magnetic moments are large in all three materials, we can assume the atoms are close to the high-spin states for simplicity. In the above effective model, we take the spin values to be the high spin of the atoms. For example, the Cr^{2+} ion has four electrons, so the spin $S = 2$. Similarly, we take $S = \frac{5}{2}$ for the Mn^{2+} ion and $S = 2$ for the Fe^{2+} ion.

In the case of $U = 0$ eV, our calculated J_2/J_1 value of $BaCr_2As_2$ is -0.74. It is very close to -0.85, which is given in

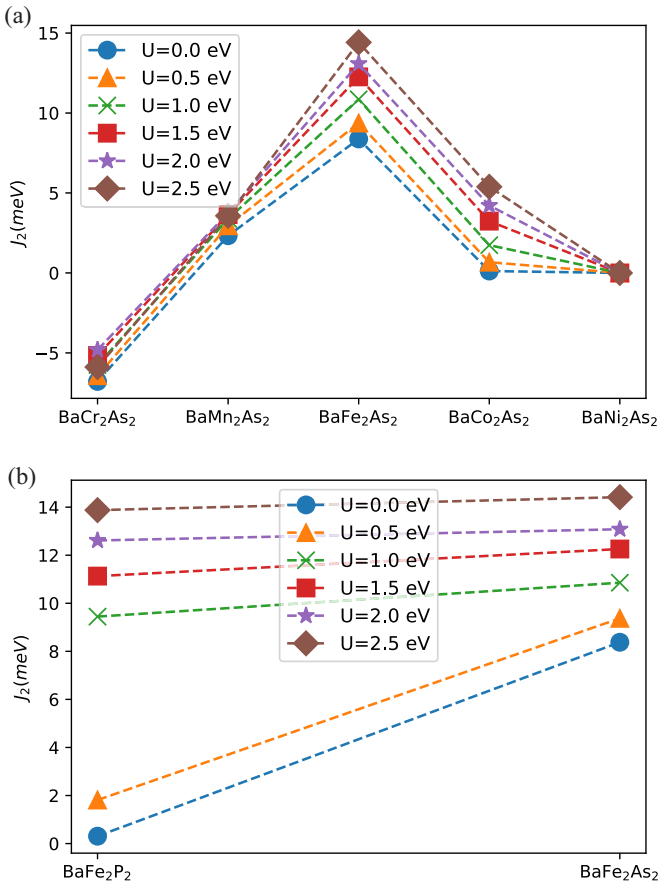

FIG. 3. The J_2 magnetic exchange coupling constants of (a) BaM_2As_2 (M = Cr, Mn, Fe, Co, Ni) and (b) $BaFe_2B_2$ (B = P, As), which are extracted from the GGA + U calculations with the values U = (0.0,0.5,1.0,1.5,2.0,2.5) eV.

a previous study [43]. Our results show that $J_1 > 0$ and $J_2 < 0$ in all U values, which suggests that $BaCr_2As_2$ has G-type AFM order. This result is the same as others' calculations [43,54] and the powder neutron diffraction experiment [44]. In $BaMn_2As_2$, our calculated exchange parameters are $J_1 = 15.30$ meV, $J_2 = 2.33$ meV, and $J_z = 1.08$ meV with high-spin values for $U = 0$ eV, which are very close to the values given in the previous calculation [42]. We also find that $J_1/J_2 < \frac{1}{2}$, which suggests that $BaMn_2As_2$ has G-type AFM order. The neutron diffraction experiment also shows that the ordered moment is $3.88(4)\mu_B$ [26]. Our results indicate that the ordered moment is $3.856\mu_B$ in the G-type state with $U = 1.5$ eV. In the case of $U = 0$ eV, our calculated exchange parameters are $J_1S^2 = 31.39$ meV and $J_2S^2 = 33.51$ meV for $BaFe_2As_2$, which are similar to the values $J_1S^2 = 25.5$ meV and $J_2S^2 = 33.8$ meV given in the previous calculations [46]. $J_1/J_2 > \frac{1}{2}$ in all U values, which suggests that $BaFe_2As_2$ has a C-type AFM order state. These results are consistent with the neutron diffraction experiment measurements [55].

The existence of large NNN AFM exchange couplings in iron-based materials, namely, J_2, is the key difference separating them from Cr/Mn-based counterparts [19]. Differing from the NN exchange couplings J_1, which stem from the direct exchange mechanism, the J_2 exchange couplings are mainly

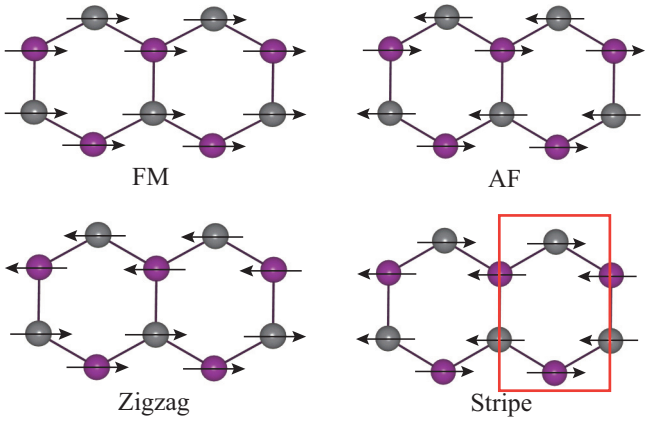

FIG. 4. Sketch of four collinear magnetic states: the FM states, the AFM state, the zigzag state, and the stripe state. The red frame indicates the magnetic unit cell in the GGA + U calculations of these magnetic structures.

contributed by the superexchange mechanism through the d-p coupling. In Fig. 3, we plot J_2 exchange coupling constants as a function of transition metal elements. Figure 3(a) shows BaM_2As_2 (M = Cr, Mn, Fe, Co, Ni), and Fig. 3(b) shows $BaFe_2B_2$ (B = P, As). It is clear that significant AFM J_2 exists only in iron-based materials. This result is strong support for the viewpoint that high-temperature superconductivity in iron-based superconductors is directly tied to the AFM J_2 [19].

IV. THE MAGNETISM IN HEXAGONAL 122 TRANSITION METAL PNICTIDES

In this section, we use the same method as in the previous section to study the magnetic properties of CaM_2B_2 (M = Cr, Mn, Fe, Co, Ni; B = As, P) with hexagonal structure. We consider four possible collinear magnetic states, the FM state, the AFM state, the zigzag state, and the stripe state, which are shown in Fig. 4. It is also reasonable to assume that the magnetic properties can be approximately described by the J_1-J_2-J_3 Heisenberg model [36,38,56], which is well studied on the honeycomb lattice [57–59]. The above four collinear magnetic states are contained in the classical phase diagram of the model on the honeycomb lattice. The coupling between the layers, namely, J_z, is ignored here as it has a different order of magnitude.

$$H = J_1 \sum_{\langle ij \rangle} \vec{S}_i \cdot \vec{S}_j + J_2 \sum_{\langle\langle ij \rangle\rangle} \vec{S}_i \cdot \vec{S}_j + J_3 \sum_{\langle\langle\langle ij \rangle\rangle\rangle} \vec{S}_i \cdot \vec{S}_j, \quad (3)$$

where $\langle ij \rangle$, $\langle\langle ij \rangle\rangle$, and $\langle\langle\langle ij \rangle\rangle\rangle$ denote the summation over the NN, NNN, and third NN, respectively. $\vec{S}_i$ is the spin operator for the ith site, and J_3 is the third-NN exchange coupling constant. The classical energies of the above magnetic states are

$$\begin{aligned} E_{\mathrm{FM}} &= NS^2(6J_1 + 12J_2 + 6J_3)/4 + E_0, \\ E_{\mathrm{AFM}} &= NS^2(-6J_1 + 12J_2 - 6J_3)/4 + E_0, \\ E_{\mathrm{zigzag}} &= NS^2(2J_1 - 4J_2 - 6J_3)/4 + E_0, \\ E_{\mathrm{stripe}} &= NS^2(-2J_1 - 4J_2 + 6J_3)/4 + E_0, \end{aligned} \quad (4)$$

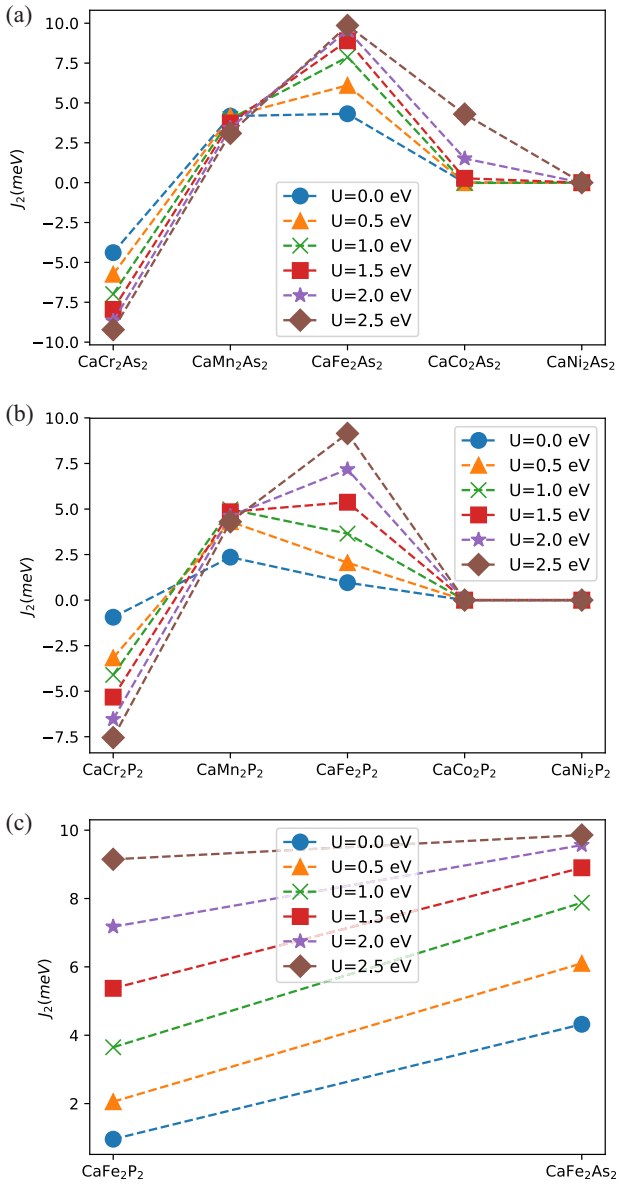

FIG. 5. The J_2 exchange coupling parameters in (a) CaM_2As_2 (M = Cr, Mn, Fe, Co, Ni), (b) CaM_2P_2 (M = Cr, Mn, Fe, Co, Ni), and (c) $CaFe_2B_2$ (B = P, As), which are extracted from the GGA + U calculations with the values U = (0.0,0.5,1.0,1.5,2.0,2.5) eV.

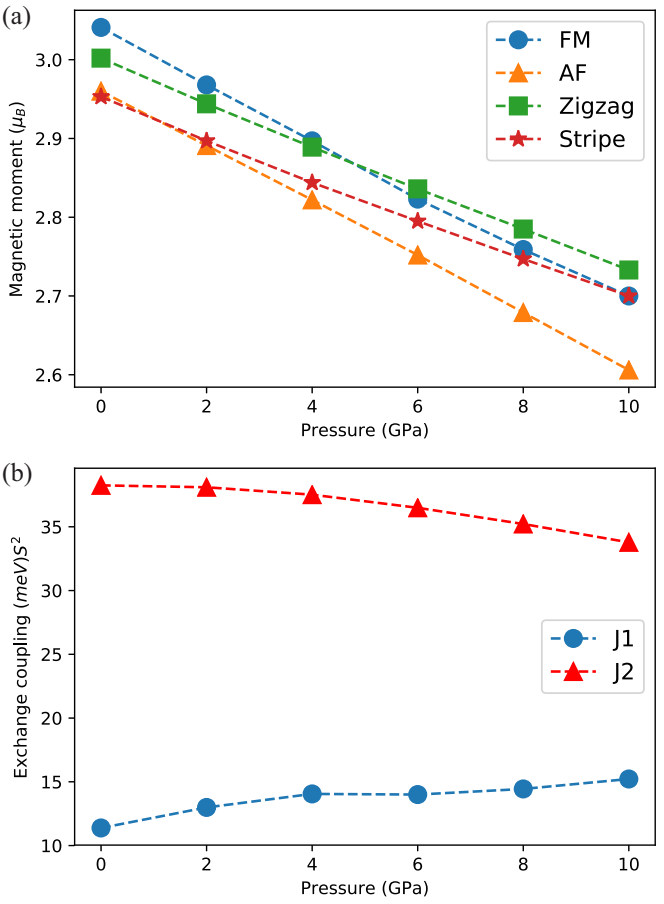

FIG. 6. (a) The magnetic moments as functions of pressure; (b) the superexchange antiferromagnetic interaction constants J_1 and J_2 as a function of the pressure for $CaFe_2As_2$.

where E_0 is the energy of the nonmagnetic state.

We calculated the magnetic moments and the total energies of the above magnetic states with GGA + U. If the calculated local magnetic moments on the M site are very close to each other, we can extract the magnetic exchange coupling constants using Eqs. (4). For the S values, we also adopt the high-spin values, which are shown in Sec. III.

Our calculations suggest that the magnetism in the hexagonal materials has a trend very similar to those of the tetragonal counterparts in the previous section. In $CaCr_2As_2$ the average moments of the four magnetic states range from $3.2\mu_B$ to $3.7\mu_B$, and the value increases when U increases. The moments vary weakly for the above four magnetic states in each U. The case for $CaCr_2P_2$ is very similar to the case for $CaCr_2As_2$, but the moment values are a little smaller than the values for $CaCr_2As_2$, in which the average moments of the four magnetic states are in the range $3.0\mu_B$–$3.6\mu_B$, except that the average moment is $2.47\mu_B$ at $U = 0$ eV. The average moments at different U are in the range $3.7\mu_B$–$4.2\mu_B$ ($3.4\mu_B$–$4.1\mu_B$) for $CaMn_2As_2$ ($CaMn_2P_2$) and $2.3\mu_B$–$3.1\mu_B$ ($1.6\mu_B$–$2.7\mu_B$) for $CaFe_2As_2$ ($CaFe_2P_2$). For $CaCo_2As_2$ ($CaCo_2P_2$) the moments are very small, and the moments vary more strongly than those for $CaCr_2As_2$ ($CaCr_2P_2$), $CaMn_2As_2$ ($CaMn_2P_2$), and $CaFe_2As_2$ ($CaFe_2P_2$). Finally, for $CaNi_2As_2$ ($CaNi_2P_2$) the moments are zero within the range of error $0.005\mu_B$, and the energies are near degeneracy. Note that our DFT results show that the AFM state has the lowest energy in $CaMn_2As_2$, which is consistent with the experiment result [33]. Following the same procedure as in the previous section, we can extract the magnetic exchange coupling parameters using Eqs. (4) quite accurately for $CaCr_2As_2$ ($CaCr_2P_2$), $CaMn_2As_2$ ($CaCr_2P_2$), and $CaFe_2As_2$ ($CaCr_2P_2$). However, the calculated exchange parameters are not accurate for $CaCo_2As_2$ ($CaCo_2P_2$) due to small magnetic moments, and the calculated magnetic exchange parameters for $CaNi_2As_2$ ($CaNi_2P_2$) are zero. The results are summarized in Fig. 5.

We can also find that J_2 is AFM and reaches the maximum in $CaFe_2As_2$, and it is small and even ferromagnetic in the Cr/Mn-based counterparts. In $CaFe_2P_2$, J_2 exchange is AFM

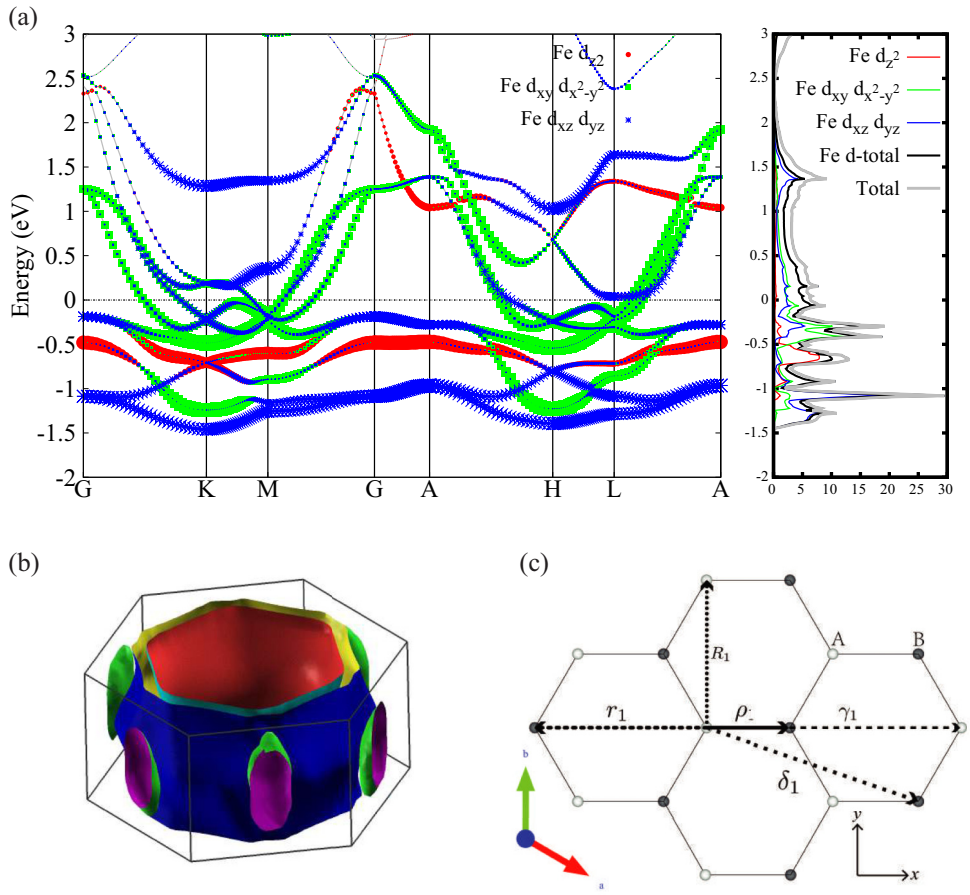

FIG. 7. (a) Band structure and density of states and (b) Fermi surface of $CaFe_2As_2$ with the optimized structural parameters in the paramagnetic state. (c) Sketch of the iron lattice: ρ_1 is the NN bond, R_1 is the NNN bond, r_1 is the third-NN bond, δ_1 is the fourth-NN bond, and γ_1 is the fifth-NN bond. The white dots denote the A sublattice, and the gray dots denotes the B sublattice.

and significant when $U \geq 1.5$ eV. J_2 is also larger in $CaFe_2As_2$ than in $CaFe_2P_2$ for the same value of U as shown in Fig. 5.

In summary, we find that the trend of the magnetism in the hexagonal materials from Cr to Ni based is very similar to those of the tetragonal counterparts. The strong AFM exchange coupling between two NNN transition metal atoms exists only in Fe-based materials. As we will show later, the presence of strong NNN AFM in iron-based materials is the result of the existence of two near-half-filling bands that are attributed to the t_{2g} d orbitals with a large d-p coupling to mediate superexchange AFM couplings.

V. PRESSURE EFFECT ON MAGNETISM

Both magnetism and superconductivity in the tetragonal iron-based superconductors are known to be sensitive to external pressure [60–62]. Here we investigate that pressure effect on the magnetism of the hexagonal structure $CaFe_2As_2$.

We relax the lattice constants and internal atomic positions with the GGA + U method ($U = 1.5$ eV) in the AFM ordered state under pressure. Then we use the optimized structural parameters to calculate the energies of the above four magnetic states with $U = 2$ eV. Using the same method as in Sec. IV, we can get the magnetic moments of the above four magnetic states and the exchange coupling parameters. Figure 6(a) shows the pressure dependence of the magnetic moments for FM, AFM, zigzag, and stripe states of $CaFe_2As_2$. The magnetic moments in the magnetic states decrease almost linearly with pressure. The magnetic moments are larger than $2\mu_B$ when the pressure is in the range 0–10 GPa. Figure 6(b) shows the change in the exchange coupling constants J_1 and J_2 as a function of the pressure. We find that both J_1 and J_2 are very robust against pressure. J_1 increases slightly, while J_2 only slightly decreases under increasing pressure.

These results are similar to those in the tetragonal AFe_2As_2 (A = Ca, Sr, Ba) [46]. The only difference is that the value of J_1 decreases in the latter under increasing pressure.

VI. ELECTRONIC STRUCTURE ON THE HEXAGONAL $CaFe_2As_2$

The electronic structure of $CaFe_2As_2$ in the paramagnetic state, including the band structure, density of states (DOS), and Fermi surface of $CaFe_2As_2$ with optimized structural parameters, is shown in Fig. 7. As shown in Figs. 7(a) and 7(b), there are three Fermi surface sheets, contributed by the three bands crossing the Fermi energy. Among them, the two big quasi-two-dimensional cylinderlike Fermi surface sheets centered around the Γ point are electron pockets. The remaining one centered around the M point forms a small

three-dimensional Fermi surface. These pockets are attributed to the $3d$ orbitals of Fe, which are located from -1.5 to 2.5 eV, as shown in Fig. 7(a). If we ignore the couplings between FeAs layers along the z direction, the electronic structure simply includes the first two electron pockets.

We can also notice some intriguing features in the distribution of the five Fe $3d$ orbitals in the electronic band structure. In the hexagonal lattice structure, the three t_{2g} d orbitals in the tetrahedron $FeAs_4$, which have higher energy than the e_g orbitals, include d_{z^2} and two other orbitals which are formed by linear combinations of the other four d orbitals in which d_{xy/x^2-y^2} carry more weight than $d_{xz/yz}$. From Fig. 7(a), we notice that the DOS of the d_{z^2} orbital near the Fermi energy is almost zero. This feature can be understood as follows. The distance between two NN Fe atoms is very short, which is about 2.902 Å. The distance between two NNN Fe atoms is about 4.086 Å. Due to the short NN Fe-Fe distance, the d_{z^2} orbitals in the two Fe atoms strongly couple to each other and form two molecular orbitals which can be called bonding and antibonding orbitals. The bonding orbital is pushed down below the Fermi energy, while the antibonding orbital is pushed up above the Fermi energy. The d_{z^2} orbital is similar to the $d_{x^2-y^2}$ orbital in tetrahedral iron-based superconductors [18,19]. Near the Fermi level, the d_{xy/x^2-y^2} orbitals have the most weight. This finding is consistent with the presence of the large AFM J_2 obtained for the iron materials but not others in the previous section because the d_{xy/x^2-y^2} orbitals have larger in-plane coupling to p orbitals of As than the other orbitals.

We can construct a microscopic electronic model to capture the band structure of $CaFe_2As_2$ by using maximally localized Wannier orbital calculations [63,64]. These maximally localized Wannier functions, centered at the Fe site in the unit cell, have five orbitals (orbital 1: $d_{3z^2-r^2}$, 2: d_{xz}, 3: d_{yz}, 4: $d_{x^2-y^2}$, 5: d_{xy}). Thus, ten orbitals are needed to describe the tight-binding model. As shown in Fig. 7(a), the band dispersion is very similar between the $k_z = 0$ plane and the $k_z = \pi$ plane, except the d_{z^2} orbital is above the Fermi level. This result suggests that the electronic physics is quasi-two-dimensional, similar to both cuprates and iron-based superconductors in which the intrinsic interesting physics is known to be two-dimensional [18,19,65,66]. Therefore, for simplicity, we construct a two-dimensional model with in-plane tight-binding couplings,

$$H = \sum_{i\vec{\Delta}} \sum_{mn} \sum_{\mu\nu\sigma} t^{mn}_{i\vec{\Delta},\mu\nu} c^{\dagger}_{i,m\mu\sigma} c_{i+\vec{\Delta},n\nu\sigma} + \sum_{im\mu} (\varepsilon_\mu - \mu) n_{im\mu}, \tag{5}$$

where $t^{mn}_{i\vec{\Delta},\mu\nu}$ are in-plain hopping integrals, $\vec{\Delta}$ is the hopping vector, $m/n = A,B$ labels the sublattice, and $\mu/\nu = 1,\ldots,5$ labels the orbital. $c^{\dagger}_{i,m\mu\sigma}$ creates an electron with spin σ on the μth orbital at site i of the mth sublattice, and $n_{im\mu} = c^{\dagger}_{im\mu} c_{im\mu}$. The on-site energies for the five orbitals are $(\varepsilon_1,\varepsilon_2,\varepsilon_3,\varepsilon_4,\varepsilon_5) = (4.103,3.967,3.967,4.077,4.077)$ eV, and the Fermi energy $\mu = 4.116$ eV. Some in-plain hopping integrals $t^{mn}_{i\vec{\Delta},\mu\nu}$ are provided in Table IV; other hopping integrals can be obtained by applying symmetry transformations according to the point group D_{3d}. For the NN bonds and the third-NN bonds, we can apply the symmetry transformations including inversion through the bond center, time reversal, and C_2 rotations. For the fourth-NN bonds, there are no C_2 rotations. Explicitly, the symmetry transformations lead to $t^{AB}_{\rho_1,\nu\mu} = t^{AB}_{\rho_1,\mu\nu}$, $t^{AB}_{r_1,\nu\mu} = t^{AB}_{r_1,\mu\nu}$, and $t^{AB}_{\delta_1,\nu\mu} = t^{AB}_{\delta_1,\mu\nu}$. The hopping integrals of the other bonds can be obtained by applying the C_3 rotations along the z direction for the NN bonds and the third-NN bonds. For the fourth-NN bonds, the additional σ_v symmetry operations are needed. The hopping integrals for the other NNN bonds and the fifth-NN bonds can also be determined by applying the C_3 rotations along the z direction and the σ_v symmetry transformation. We can rotate the whole lattice by a C_2 rotation along the z direction, then translate the lattice in the direction with the vector A to B. In this case, the sites in the new lattice B locate at the A sites of the original lattice. Then the bond direction for the B site is opposite the bond direction for the A site of the original lattice. The C_2 rotation symmetry transformation lead to $t^{BB}_{R_i,\nu\mu} = t^{AA}_{-R_i,\mu\nu}$ and $t^{BB}_{\gamma_i,\nu\mu} = t^{AA}_{-\gamma_i,\mu\nu}$, in which R_i denote all the second-NN bonds and γ_i denote all the fifth-NN bonds.

TABLE IV. A subset of hopping integrals $t^{mn}_{i\vec{\Delta},\mu\nu}$ up to the fifth NN (units are eV). $\vec{\Delta}$ is the hopping vector, $m/n = A,B$ are sublattice indices, and $\mu/\nu = 1,\ldots,5$ denote orbitals. ρ_1 is the NN bond, R_1 is the NNN bond, r_1 is the third-NN bond, δ_1 is the fourth-NN bond, and γ_1 is the fifth-NN bond. Other hopping integrals can be obtained by applying the symmetry operations as described in the main text.

	NN $\vec{\Delta} = \rho_1$ $A \to B$	NNN $\vec{\Delta} = R_1$ $A \to A$	Third NN $\vec{\Delta} = r_1$ $A \to B$	Fourth NN $\vec{\Delta} = \delta_1$ $A \to B$	Fifth NN $\vec{\Delta} = \gamma_1$ $A \to A$
(1,1)	−0.33	0.10	−0.02	0.00	−0.00
(1,2)	0.14	0.05	0.00	−0.01	0.00
(1,3)	0	0.07	0	0.01	0
(1,4)	0.15	0.03	0.01	0.02	−0.01
(1,5)	0	−0.07	0	0.01	0
(2,2)	−0.69	−0.05	0.00	−0.03	−0.01
(2,3)	0	−0.03	0	0.00	0
(2,4)	0.04	−0.02	0.03	0.00	−0.01
(2,5)	0	−0.10	0	0.03	0
(3,3)	0.16	0.05	0.07	0.00	0.00
(3,4)	0	0.10	0	−0.01	0
(3,5)	−0.04	0.16	−0.01	0.00	0.00
(4,4)	−0.05	0.14	0.01	0.01	0.02
(4,5)	0	−0.11	0	0.01	0
(5,5)	0.18	0.19	0.00	0.01	0.02

VII. POSSIBLE SUPERCONDUCTIVITY FOR HEXAGONAL $CaFe_2As_2$

In this section, we discuss possible superconducting states in the hexagonal iron-based materials under the assumption that the superexchange couplings cause superconductivity.

Since the crystal structure of $CaFe_2As_2$ belongs to the point group D_{3d}, the pairing symmetry of $CaFe_2As_2$ can be classified according to the irreducible representations of the D_{3d} point group. Moreover, only even-parity spin-singlet pairing is allowed if the superconductivity is driven by the AFM exchange couplings. In this case, there are two possible superconducting states with A_{1g} (extended s wave) and E_g (d wave). For the E_g d-wave states, there are two

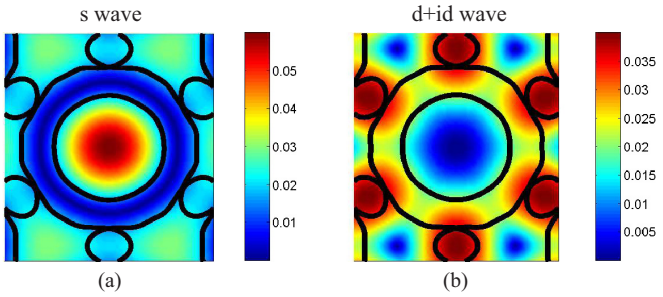

FIG. 8. The overlap between the Fermi surfaces (black lines) and the superconducting gap distribution for $CaFe_2As_2$ in the first Brillouin zone (BZ) in the $k_z = 0$ plane for the extended (a) s-wave and (a) $(d + id)$-wave cases. The s-wave order parameter in k space has a momentum form factor $\Delta(\boldsymbol{k}) = \Delta(2\cos\frac{\sqrt{3}}{2}k_x\cos\frac{1}{2}k_y + \cos k_y)$, and the $(d + id)$-wave order parameter has $\Delta(\boldsymbol{k}) = \Delta(\cos k_y - \cos\frac{\sqrt{3}}{2}k_x\cos\frac{1}{2}k_y + i\sqrt{3}\sin\frac{\sqrt{3}}{2}k_x\sin\frac{1}{2}k_y)$. The color bar labels the amplitude of the SC gap when $\Delta = 0.02$.

degenerate states. The superconducting condensation energy can be further lowered by forming the time-reversal symmetry-breaking $(d \pm id)$-wave states [18,67]. Thus, we just need to compare the energies between the extended s-wave and $(d \pm id)$-wave states.

A selection rule to determine the superconducting state, which we refer as the Hu-Ding principle, has been proposed [68,69] to unify the d-wave pairing in cuprates and s-wave pairing in iron-based superconductors. The principle states that in order to generate high-T_c superconductivity, the momentum space form factor of the superconducting pairing gap function which is determined by the AFM superexchange couplings must have large overlap with Fermi surfaces. The most favored pairing symmetry is the one which has the largest overlap strength [68]. The overlap strength can be defined as

$$W = \int\int dk_x dk_y |\Delta_{\boldsymbol{k}}|^2 \delta(\epsilon_{\boldsymbol{k}} - \mu), \tag{6}$$

where $\Delta_{\boldsymbol{k}}$ is the momentum space SC gap function. In our case, the gap function stems from the NNN AFM superexchange couplings. For the extended s-wave, $\Delta(\boldsymbol{k}) = \Delta(2\cos\frac{\sqrt{3}}{2}k_x\cos\frac{1}{2}k_y + \cos k_y)$, and for the $(d + id)$-wave order parameter $\Delta(\boldsymbol{k}) = \Delta(\cos k_y - \cos\frac{\sqrt{3}}{2}k_x\cos\frac{1}{2}k_y + i\sqrt{3}\sin\frac{\sqrt{3}}{2}k_x\sin\frac{1}{2}k_y)$, where Δ is a constant. In Fig. 8, we plot the overlap strength for both the s-wave [Fig. 8(a)] and $(d + id)$-wave [Fig. 8(b)] cases for 0.2 electron doping. The overlap strength for the $d \pm id$ wave is 2.85 times larger than the s-wave case (with an energy cutoff 0.05 eV from the Fermi energy), so the most favored pairing symmetry for the hexagonal $CaFe_2As_2$ is the $d + id$ wave. Therefore, the $d \pm id$ superconducting state is favored.

VIII. DISCUSSION AND CONCLUSION

In summary, we have shown that the hexagonal transition metal pnictides have a trend in magnetic exchange interactions very similar to their tetragonal counterparts. In both cases, the iron-based materials maximize the NNN antiferromagnetic interactions, and those d orbitals which are responsible for the largest superexchange interactions dominate near Fermi surfaces. The superexchange interactions make the hexagonal iron materials extremely magnetic frustrated systems and can also lead to $d + id$ superconducting ground states upon doping. As the energy scales of the NNN AFM superexchange couplings in both hexagonal and tetragonal iron materials are close to each other, we expect that the hexagonal materials can host high-T_c superconductivity, just like their tetragonal counterparts.

Although the hexagonal Mn-based pnictides have been successfully synthesized, the iron-based counterparts have not been obtained yet. However, it is worth mentioning that the iron-based hexagonal materials are stable in our theoretical investigation. Their phonon spectra do not show any imaginary modes. Our study can be extended to include transition metal chalcogenides. Similar results can be expected for chalcogenides with similar hexagonal structures.

ACKNOWLEDGMENTS

We thank X. X. Wu for helpful discussions. This work is supported by the Ministry of Science and Technology of China 973 program (Grants No. 2015CB921300 and No. 2017YFA0303100), the National Science Foundation of China (Grants No. NSFC-1190020, No. 11534014, and No. 11334012), and the Strategic Priority Research Program of CAS (Grant No. XDB07000000).

[1] Y. Kamihara, T. Watanabe, M. Hirano, and H. Hosono, J. Am. Chem. Soc. **130**, 3296 (2008).
[2] P. J. Hirschfeld, M. M. Korshunov, and I. I. Mazin, Rep. Prog. Phys. **74**, 4508 (2011).
[3] J. G. Bednorz and K. A. Muller, Z. Phys. B **64**, 189 (1986).
[4] A. S. Sefat, D. J. Singh, L. H. VanBebber, Y. Mozharivskyj, M. A. McGuire, R. Jin, B. C. Sales, V. Keppens, and D. Mandrus, Phys. Rev. B **79**, 224524 (2009).
[5] D. Kasinathan, A. Ormeci, K. Koch, U. Burkhardt, W. Schnelle, A. Leithe-Jasper, and H. Rosner, New J. Phys. **11**, 025023 (2009).
[6] A. Pandey, V. K. Anand, and D. C. Johnston, Phys. Rev. B **84**, 014405 (2011).
[7] A. Pandey, R. S. Dhaka, J. Lamsal, Y. Lee, V. K. Anand, A. Kreyssig, T. W. Heitmann, R. J. McQueeney, A. I. Goldman, B. N. Harmon *et al.*, Phys. Rev. Lett. **108**, 087005 (2012).

[8] K. Ahilan, T. Imai, A. S. Sefat, and F. L. Ning, Phys. Rev. B **90**, 014520 (2014).

[9] V. K. Anand, D. G. Quirinale, Y. Lee, B. N. Harmon, Y. Furukawa, V. V. Ogloblichev, A. Huq, D. L. Abernathy, P. W. Stephens, R. J. McQueeney *et al.*, Phys. Rev. B **90**, 064517 (2014).

[10] F. Ronning, N. Kurita, E. D. Bauer, B. L. Scott, T. Park, T. Klimczuk, R. Movshovich, and J. D. Thompson, J. Phys. Condens. Matter **20**, 342203 (2008).

[11] P. Zhang and H.-f. Zhai, Condens. Matter **2**, 28 (2017).

[12] B. Saparov and A. S. Sefat, J. Solid State Chem. **191**, 213 (2012).

[13] V. K. Anand, P. K. Perera, A. Pandey, R. J. Goetsch, A. Kreyssig, and D. C. Johnston, Phys. Rev. B **85**, 214523 (2012).

[14] P. Dai, Rev. Mod. Phys. **87**, 855 (2015).

[15] K. J. Seo, B. A. Bernevig, and J. P. Hu, Phys. Rev. Lett. **101**, 206404 (2008).

[16] C. Fang, Y. L. Wu, R. Thomale, B. A. Bernevig, and J. P. Hu, Phys. Rev. X **1**, 011009 (2011).

[17] J. Hu and J. Yuan, Front. Phys. **11**, 117404 (2016).

[18] J. Hu, C. Le, and X. Wu, Phys. Rev. X **5**, 041012 (2015).

[19] J. Hu, Sci. Bull. **61**, 561 (2016).

[20] G. Kresse and J. Hafner, Phys. Rev. B **47**, 558 (1993).

[21] G. Kresse and J. Furthmüller, Comput. Mater. Sci. **6**, 15 (1996).

[22] G. Kresse and J. Furthmüller, Phys. Rev. B **54**, 11169 (1996).

[23] J. P. Perdew, K. Burke, and M. Ernzerhof, Phys. Rev. Lett. **78**, 1396 (1997).

[24] S. L. Dudarev, G. A. Botton, S. Y. Savrasov, C. J. Humphreys, and A. P. Sutton, Phys. Rev. B **57**, 1505 (1998).

[25] M. Pfisterer and G. Nagorsen, Z. Naturforsch. **35b**, 703 (1980).

[26] Y. Singh, M. A. Green, Q. Huang, A. Kreyssig, R. J. McQueeney, D. C. Johnston, and A. I. Goldman, Phys. Rev. B **80**, 100403 (2009).

[27] M. Rotter, M. Tegel, D. Johrendt, I. Schellenberg, W. Hermes, and R. Pöttgen, Phys. Rev. B **78**, 020503 (2008).

[28] B. J. Arnold, S. Kasahara, A. I. Coldea, T. Terashima, Y. Matsuda, T. Shibauchi, and A. Carrington, Phys. Rev. B **83**, 220504 (2011).

[29] E. Brechtel, G. Cordier, and H. Schaefer, Z. Naturforsch. **33b**, 820 (1978).

[30] A. Mewis, Z. Naturforsch. **33b**, 606 (1978).

[31] S. L. Brock, J. E. Greedan, and S. M. Kauzlarich, J. Solid State Chem. **113**, 303 (1994).

[32] S. Bobev, J. Merz, A. Lima, V. Fritsch, J. D. Thompson, J. L. Sarrao, M. Gillessen, and R. Dronskowski, Inorg. Chem. **45**, 4047 (2006).

[33] N. S. Sangeetha, A. Pandey, Z. A. Benson, and D. C. Johnston, Phys. Rev. B **94**, 094417 (2016).

[34] P. Das, N. S. Sangeetha, A. Pandey, Z. A. Benson, T. W. Heitmann, D. C. Johnston, A. I. Goldman, and A. Kreyssig, J. Phys. Condens. Matter **29**, 035802 (2017).

[35] J. W. Simonson, G. J. Smith, K. Post, M. Pezzoli, J. J. Kistner-Morris, D. E. McNally, J. E. Hassinger, C. S. Nelson, G. Kotliar, D. N. Basov, and M. C. Aronson, Phys. Rev. B **86**, 184430 (2012).

[36] D. E. McNally, J. W. Simonson, J. J. Kistner-Morris, G. J. Smith, J. E. Hassinger, L. DeBeer-Schmitt, A. I. Kolesnikov, I. A. Zaliznyak, and M. C. Aronson, Phys. Rev. B **91**, 180407 (2015).

[37] C. Fang, H. Yao, W. F. Tsai, J. P. Hu, and S. A. Kivelson, Phys. Rev. B **77**, 224509 (2008).

[38] C. Fang, B. A. Bernevig, and J. P. Hu, Europhys. Lett. **86**, 6 (2009).

[39] D. C. Johnston, Adv. Phys. **59**, 803 (2010).

[40] M. Holt, O. P. Sushkov, D. Stanek, and G. S. Uhrig, Phys. Rev. B **83**, 144528 (2011).

[41] D. Stanek, O. P. Sushkov, and G. S. Uhrig, Phys. Rev. B **84**, 064505 (2011).

[42] D. C. Johnston, R. J. McQueeney, B. Lake, A. Honecker, M. E. Zhitomirsky, R. Nath, Y. Furukawa, V. P. Antropov, and Y. Singh, Phys. Rev. B **84**, 094445 (2011).

[43] D. J. Singh, A. S. Sefat, M. A. McGuire, B. C. Sales, D. Mandrus, L. H. VanBebber, and V. Keppens, Phys. Rev. B **79**, 094429 (2009).

[44] K. A. Filsinger, W. Schnelle, P. Adler, G. H. Fecher, M. Reehuis, A. Hoser, J.-U. Hoffmann, P. Werner, M. Greenblatt, and C. Felser, Phys. Rev. B **95**, 184414 (2017).

[45] J. An, A. S. Sefat, D. J. Singh, and M.-H. Du, Phys. Rev. B **79**, 075120 (2009).

[46] F.-j. Ma, Z.-y. Lu, and T. Xiang, Front. Phys. China **5**, 150 (2010).

[47] G. Xu, H. Zhang, X. Dai, and Z. Fang, Europhys. Lett. **84**, 67015 (2008).

[48] M. Zbiri, H. Schober, M. R. Johnson, S. Rols, R. Mittal, Y. Su, M. Rotter, and D. Johrendt, Phys. Rev. B **79**, 064511 (2009).

[49] Z. P. Yin and W. E. Pickett, Phys. Rev. B **80**, 144522 (2009).

[50] L. Boeri, M. Calandra, I. I. Mazin, O. V. Dolgov, and F. Mauri, Phys. Rev. B **82**, 020506 (2010).

[51] M. J. Han, Q. Yin, W. E. Pickett, and S. Y. Savrasov, Phys. Rev. Lett. **102**, 107003 (2009).

[52] A. S. Sefat, D. J. Singh, R. Jin, M. A. McGuire, B. C. Sales, and D. Mandrus, Phys. Rev. B **79**, 024512 (2009).

[53] B. Zhou, M. Xu, Y. Zhang, G. Xu, C. He, L. X. Yang, F. Chen, B. P. Xie, X.-Y. Cui, M. Arita *et al.*, Phys. Rev. B **83**, 035110 (2011).

[54] P. Richard, A. van Roekeghem, B. Q. Lv, T. Qian, T. K. Kim, M. Hoesch, J.-P. Hu, A. S. Sefat, S. Biermann, and H. Ding, Phys. Rev. B **95**, 184516 (2017).

[55] Q. Huang, Y. Qiu, W. Bao, M. A. Green, J. W. Lynn, Y. C. Gasparovic, T. Wu, G. Wu, and X. H. Chen, Phys. Rev. Lett. **101**, 257003 (2008).

[56] J. Hu, B. Xu, W. Liu, N.-N. Hao, and Y. Wang, Phys. Rev. B **85**, 144403 (2012).

[57] E. Rastelli, A. Tassi, and L. Reatto, Phys. B+C (Amsterdam) **97**, 1 (1979).

[58] J. B. Fouet, P. Sindzingre, and C. Lhuillier, Eur. Phys. J. B **20**, 241 (2001).

[59] J. Oitmaa and R. R. P. Singh, Phys. Rev. B **84**, 094424 (2011).

[60] M. S. Torikachvili, S. L. Bud'ko, N. Ni, and P. C. Canfield, Phys. Rev. Lett. **101**, 057006 (2008).

[61] T. Park, E. Park, H. Lee, T. Klimczuk, E. D. Bauer, F. Ronning, and J. D. Thompson, J. Phys. Condens. Matter **20**, 322204 (2008).

[62] P. L. Alireza, Y. T. C. Ko, J. Gillett, C. M. Petrone, J. M. Cole, G. G. Lonzarich, and S. E. Sebastian, J. Phys. Condens. Matter **21**, 012208 (2009).
[63] N. Marzari and D. Vanderbilt, Phys. Rev. B **56**, 12847 (1997).
[64] I. Souza, N. Marzari, and D. Vanderbilt, Phys. Rev. B **65**, 035109 (2001).
[65] K. Kuroki, S. Onari, R. Arita, H. Usui, Y. Tanaka, H. Kontani, and H. Aoki, Phys. Rev. Lett. **101**, 087004 (2008).
[66] W. E. Pickett, Rev. Mod. Phys. **61**, 433 (1989).
[67] M. H. Fischer, T. Neupert, C. Platt, A. P. Schnyder, W. Hanke, J. Goryo, R. Thomale, and M. Sigrist, Phys. Rev. B **89**, 020509 (2014).
[68] J. Hu and H. Ding, Sci. Rep. **2**, 381 (2012).
[69] J. C. S. Davis and D.-H. Lee, Proc. Natl. Acad. Sci. USA **110**, 17623 (2013).